Facile Synthesis of Cadmium Doped Graphite Carbon Nitride for Photocatalytic Degradation of Tetracycline Under Visible Light Irradiation

yin zhao
Hunan University
hong qin
Hunan University
ziwei wang
Hunan University
han wang
Hunan University
yangzhuo he
Hunan University
Quyang Tian
Hunan University
Qianlan luo
Hunan University
Piao Xu (piaoxu@hnu.edu.cn)
Hunan University

Research Article

Keywords: Carbon nitride, Cadmium-doping, Tetracycline, Photodegradation

Posted Date: March 1st, 2022

DOI: https://doi.org/10.21203/rs.3.rs-1118826/v1

Abstract

Using semiconductor photocatalysts for antibiotic contaminants degradation under visible light has become a hot topic in recent years. Herein, a novel and ingenious cadmium doped graphite phase carbon nitride (Cd-g-C_3N_4) photocatalyst was successfully constructed via 60°C oil bath method to degrade tetracycline. Experimental and characterization results revealed that cadmium was well doped at g-C_3N_4 surface and exhibited high intercontact with g-C_3N_4. Additionally, the introduction of cadmium significantly improved the photocatalytic activity, and the optimum degradation efficiency of 10-Cd-g-C_3N_4 reached to 98.1%, which was exceeded 2.0 times than pure g-C_3N_4 (43.9%). Meanwhile, the 10-Cd-g-C_3N_4 sample presented higher electrical conductivity, light absorption property and photogenerated electron-hole pairs migration compared with bare g-C_3N_4. Additionally, the quenching experiments and electron spin-resonance tests were exhibited holes (h^+), hydroxyl radicals (•OH) and superoxide radicals ($•O_2^-$) were main active species involved in TC degradation. Equally, the effects of various conditions on photocatalytic efficiency, such as pH, initial TC concentrations and catalyst dosage, were also researched. This work gives a reasonable point to synthesize high-efficiency and economic photocatalysts.

1. Introduction

For the past few years, researchers have been seeking suitable ways to solve the overwhelming environmental problems, caused by the continuous increase of population and energy-intensive industry (Abbott 2010; McCauley & Stephens 2012; Wang & Yang 2016). Especially, the recklessly discharged of untreated wastewater and sewage have posed a huge threat to water environment. Photocatalysis, as an environmental-friendly process, has become a significant method applied in energy and environmental remediation field (Ge et al. 2011; Liu et al. 2016; Wang et al. 2008; Zhu et al. 2017). Undoubtedly, the most important tasks in photocatalysis research are designing high-efficient, non-toxic and low-cost photocatalysts, which should include sustainable light absorption capacity, narrow band gap, controllable morphology and good redox ability (Xiang et al. 2012). Recently, metallic oxides, metallic nitrides and metallic sulfides have developed as excellent photocatalytic material to remove organic pollutants (Chan et al. 2017; Shi et al. 2018; Song et al. 2019; Wang et al. 2018b; Xiao & Jiang 2017; Xu et al. 2019). Whereas, some obvious defects have hindered their further application, such as high cost, low degradation efficiency and time-consuming (Yan et al. 2010; Yu & Wang 2015; Yuan et al. 2014; Zhang et al. 2016c; Zhao et al. 2014).

In comparison, more recently discovered carbon nitride with several covalent CN allotropes is considered as one of the most promising photocatalysts than metallic photocatalysts (Dong et al. 2012; Samanta et al. 2014; Wang et al. 2008). Among the five phases (alpha, beta, cubic, quasi-cubic and graphite phase) of carbon nitride, graphite phase carbon nitride (g-C_3N_4), as a metal-free and environmentally benign conjugated catalyst (Lu et al. 2015; Zhou et al. 2013), was received much attention and widely used in organic pollutants degradation, particularly owing to its high physicochemical stability, adjustable electronic structure, molecular tunability, suitable specific surface area and appropriate band gap for

absorbing blue light (Butchosa et al. 2014; Chai et al. 2012; Chen et al. 2020; Fan et al. 2016; Liu et al. 2015; Samanta et al. 2014; Wang et al. 2020a; Wang et al. 2019; Wang et al. 2020b; Yan et al. 2009a). Nevertheless, the disadvantages of g-C_3N_4 cannot be ignored, such as insufficient light absorption (Li et al. 2009a), low surface area and rapid recombination rate of photo-generated carriers (Chang et al. 2018; Zhang & Xia 2011), which limited the photodegradation properties.

Several strategies, including chemical doping, morphological control, electronic structural design and defects engineering have been explored to overcome the shortcomings of g-C_3N_4 and enhance the photocatalytic performance (Gao et al. 2012; Katsumata et al. 2014; Ou et al. 2015; Qi et al. 2018). Among these strategies, metal elements doping of g-C_3N_4 have been commonly exhibited much advantages and was regarded as a feasible method to improve photodegradation properties (Schwinghammer et al. 2014; Tahir et al. 2013; Thaweesak et al. 2017; Wang et al. 2018b). First of all, metal dopants can generate lone electron pairs in pure g-C_3N_4 as it interacts with the cations, accordingly, the ability to capture electrons was enhanced (Gao et al. 2013; Ong et al. 2016; Wang et al. 2009a). Simultaneously, metal doping can extend visible light absorption range, improve charge transfer efficiency, and enhance redox capacity (Jun et al. 2013; Liu et al. 2012; Samanta et al. 2014). Meanwhile, metal doping can effectively adjust the morphology and crystal phase of g-C_3N_4, consequently, the photocatalytic activity of the catalyst was enhanced by introducing oxygen vacancies or constructing heterogeneous structures (Fan et al. 2019; Gao et al. 2012; Huang et al. 2019; Zhu et al. 2017).

In this paper, an ingenious cadmium doped graphite phase carbon nitride photocatalyst was successfully constructed via 60°C oil bath method, different proportions of cadmium were introduced into porous g-C_3N_4 photocatalyst. To the best of our knowledge, there is rarely reported of cadmium doped g-C_3N_4 for photocatalytic degradation. The experimental and characterization results of photodegrading TC under visible light irradiation demonstrated that cadmium doped graphite phase carbon nitride exhibited a higher light absorption ability and surface area, fast transfer of photo-generated carriers and correspondingly improved photocatalytic performance. This study elaborated the mechanism of cadmium doping for photoactivity improvement in detail and offers an innovative viewpoint for further chemistry doped of g-C_3N_4.

2. Experimental Section

2.1. Chemicals

All the chemicals were of analytical grade. Cadmium chloride ($CdCl_2$), polyvinyl alcohol (PVA), melamine, tetracycline (TC), ethylenediaminetetraacetic acid disodium salt (EDTA-2Na), anhydrous ethanol, isopropanol (IPA), 4-hydroxy-2,2,6,6-tetramethylpiperidinyloxy (TEMPO), deionized water (H_2O), were employed without further purification.

2.2. Synthesis of g-C_3N_4

The g-C_3N_4 powder was prepared via traditional calcination method with little revision, the specific steps were as follows (Wang et al. 2021): Weighing 10 g melamine into a porcelain alumina crucible (50 ml), covered with tin foil. Then the crucible was placed into muff furnace with a heating rate of 10°C /min, kept at 550°C for 3 h. After the porcelain alumina crucible was cooled down to room temperature, the obtained g-C_3N_4 powder was grounded and collected for further use.

2.3. Synthesis of Cd-g-C_3N_4

All Cd doped g-C_3N_4 samples was prepared through the thermal polymerization of melamine in the presence of $CdCl_2$. 1.0 g g-C_3N_4 sample was taken and dissolved in 20 mL of ethanol/H_2O solution (15/5, vol/vol), then put different amounts of $CdCl_2$ into the solution. After ultrasound for half an hour, the solvent evaporated in an oil bath under magnetic agitation at 60°C. Whereafter, the remaining solids were placed in a petri dish, covered with plastic wrap and desiccated in vacuum drying oven at 60°C for 24 h, when cooled to room temperature, the obtained samples were poured into a mortar to thoroughly ground. Then the samples were placed into muff furnace with a heating rate of 10°C/ min, kept at 550°C for 3 h. When the product was static cooled, the product was marked as X-Cd-g-C_3N_4 photocatalysts (X = 5, 10, 15) with different cadmium chloride contents. The cadmium chloride contents in carbon nitride material samples were listed in Table S1 and Scheme S1 illustrated the brief diagram of 10-Cd-g-C_3N_4 prepared process.

2.4. Characterization

X-ray diffraction (XRD) was recorded by D8 advance via Cu-Kα radiation, the scan ranges of 2θ extended from 10 º to 80 º with a scan speed of 8°/min. The morphological structure was obtained on JSM-7800F scanning electron microscopy (SEM). Escalab 250Xi spectrometer via Al Kα X-ray source was employed to measure X-ray photoelectron spectroscopy (XPS). The morphologies of the catalyst were observed through Jeol 2100F transmission electron microscopy (TEM). The photoluminescence spectra (PL) spectra were investigated by Fluoromax-4 spectrofluorometer at 380 nm excitation wavelength. Fourier transform infrared spectroscopy (FT-IR) was measured by Bruker spectrometer, with the wavenumber ranging from 500 to 4000 cm^{-1}. Ultraviolet–visible diffuse reflectance absorption spectroscopy (UV-Vis DRS) was performed on Cary 300 UV-Vis spectrophotometer, scanning from 200 ~ 800 nm. The Brunauer–Emmett–Teller (BET) surface area was carried out by Micromeritics ASAP2460. Electrochemical impedance spectroscopy (ESR) was analyzed by Bruker a300. The total organic carbon (TOC) was tested via Analytikjena multi N/C 2100. The chemical element compositions were analyzed by the energy dispersive spectroscopy (EDS) mapping images, captured on a Zeiss Sigma 300 atomic resolution analytical microscope.

2.5. Photocatalytic process

A 300 W Xenon lamp with 420 nm pass filter was employed to simulate sunlight for catalytic process. Typically, 0.04 g catalyst was weighed in a 100 mL beaker, 50 mL TC solution at 10 mg/L was poured in the beaker and stirred at 450 rpm/s for photocatalysis studies. In order to eliminated the effect of

adsorption, we placed the mixture solutions in the dark and stirred for 0.5 hour until the adsorption-desorption equilibrium. During the light source was added, TC suspension was collected every 10 min with a 0.22 μm filter membrane. Then the concentration of suspension was tested by UV-Vis spectrophotometer with wavelength at 357 nm.

2.6. Photoelectrochemical process

The photoelectrochemical (PEC) test of catalyst was conducted on CHI0-660D workstation. A 300 W Xenon lamp with 420 nm pass filter was used as light source. The PEC performance of g-C_3N_4 and 10-Cd-g-C_3N_4 were evaluated using a normal three-electrode system with 0.2 M Na_2SO_4 solution. In the three electrodes system, Ag/AgCl electrode was reference electrode, Pt electrode was counter electrode and working electrode was fluorine-doped tin oxide (FTO) with diluted catalyst. The adhered process was depicted as follows: FTO was firstly ultrasonic cleaned in ethanol, acetone and deionized water for three times, respectively. Secondly, 10 mg catalyst was uniformly immersed into 150 uL naphthol for ultrasonic oscillation. Finally, 100 μL suspension was evenly dropped onto FTO and dried at 120°C.

3. Results And Discussion

3.1. Structure and morphology

The structure and crystalline phase were analyzed by XRD. Fig. 1a confirmed g-C_3N_4 has two diffraction peaks at vicinity of 12.9° (100) and 27.5° (002), which were in good agreement with the standard XRD pattern of graphitic carbon nitride (JCPDS 87-1526). The peak at 12.9° was confirmed by the in-planar tri-s-triazine structural ordering of the conjugated aromatic system, and the peak at 27.5° was represented the inter-planar periodic lamellar ordering of typical graphite-like carbon nitride (Li et al. 2016). According to Bragg's Law, the distance between the in-plane layers was about 0.69 nm, and the distance between the inter-planar layers was about 0.33 nm (Lu et al. 2015; Zou et al. 2019). On the contrary, the intensities of both two peaks were significantly abated, and the peaks were minor shifted in 10-Cd-g-C_3N_4 samples, indicating that the Cd elements incorporated into the g-C_3N_4 lattice and resulting to the reduced hydrogen bond effect (Sher et al. 2021), as a consequence, the distance between the inter-planar layers of g-C_3N_4 was increased (Thaweesak et al. 2017; Yu et al. 2016). These findings confirmed the successful doping of Cd, and the introduction of Cd decreased the crystallinity of g-C_3N_4 sample (Abu Hanif et al. 2021). Apparently, there were no peak of cadmium in 10-Cd-g-C_3N_4 sample, which was due to the small content of cadmium and high dispersion in solution (Jia et al. 2019; Wang et al. 2020b).

The functional groups in the g-C_3N_4 and 10-Cd-g-C_3N_4 were determined by FT-IR. As illustrated in Fig. 1b, the pure g-C_3N_4 presented numerous absorption bands. The peak at 809 cm^{-1} was assigned to the typical out-of-plane bending vibration of tri-s-triazine-based structure (Liu et al. 2020), which verified the presence of triazine units (Wang et al. 2018a; Yan et al. 2009b). Analogously, five characteristic peaks were found in the region of 1200–1700 cm^{-1}, which appeared at 1245, 1327, 1412, 1573 and 1645 cm^{-1}, respectively, indicating the distinctive stretching mode of aromatic C–N heterocycle (C_6N_7) (Park et al.

2011; Sobhana S S et al. 2011). Similarly, the wide region from 3000 to 3500 cm^{-1} were ascribed to the stretching mode of the partial hydrogenation of exposed nitrogen (N-H) and the adsorbed water molecules (O-H) (Tonda et al. 2014; Wang et al. 2018a; Yan et al. 2016). Obviously, the 10-Cd-g-C_3N_4 sample exhibited almost similar FT-IR features with g-C_3N_4, indicating the primary framework of g-C_3N_4 was well preserved. Specifically, a weak peak was found in the region of 2150 cm^{-1}, which may assign to the additional stretching mode caused by the interaction of cadmium and g-C_3N_4 (Sher et al. 2021). Additionally, the stretching mode of the partial hydrogenation of exposed nitrogen (N-H) was shifted and weakened, which corresponded to the Cd dopant was incorporated into g-C_3N_4 (Yang et al. 2013; Li et al. 2016).

The morphologies of as-prepared samples were examined by SEM. Fig. 2a and Fig. 2b presented the image of pure g-C_3N_4, which were layers and porous structure piled up in an irregular manner (Narkbuakaew & Sujaridworakun 2020). Also, there were large cross-sectional area between layers, which were excellent doping sites (Sher et al. 2021). After Cd doping, 10-Cd-g-C_3N_4 sample was composed of thin layer structure stacking with scattered crystals particles Fig. 2(c-d), revealing the aggregated nanosheets of g-C_3N_4 was exfoliated, the crystallinity of g-C_3N_4 was decreased (Abu Hanif et al. 2021). Elemental mapping illustrated that Cd element was homo-dispersed at the surface of g-C_3N_4, suggested the success doping of Cd (Figure S1, supporting information). The elements weight ratio of 10-Cd-g-C_3N_4 sample were illustrated in Table S2, where the elements C was 25.73%, N was 61.98% and Cd was 12.28%, indicating the low concentration of Cd compared with others elements, which confirmed the cadmium doped on the g-C_3N_4 with a slight atomic ratio. The energy dispersive X-ray spectra (EDS) were illustrated in Fig. S1a, and only three peaks (C, N, Cd) were presented in the EDS mapping spectrum, confirming that the C, N, Cd elements were homogeneous distribution and the prepared 10-Cd-g-C_3N_4 sample was highly pure.

The detailed morphologies and microstructure were further surveyed by TEM. All the prepared samples were nanometer range particle size. As depicted in Fig. 3a and Fig. 3b, it could be apparently seen that the pure g-C_3N_4 was transparent or non-transparent, owing to the overlap of multilayered nanosheets. Simultaneously, as confirmed in Fig. 3c and Fig. 3d, the 10-Cd-g-C_3N_4 exhibited an ultrathin nanosheets structure, which was beneficial for increasing the specific surface area. Analogously, a typical silk nanosheet with smooth external surface of g-C_3N_4 was observed, which manifested that the graphene-like layers were uniformly distributed and randomly oriented. Obviously, the elemental mapping (Fig. S1 and Fig. 3(e-i)) confirmed the cadmium elements were uniform interspersing at the surface of g-C_3N_4, and exhibited high intercontact with g-C_3N_4 due to the electrostatic attraction. The results were consistent with previous study that the electron-rich Cd or CdS clusters were firmly anchored on the electron-unsaturated g-C_3N_4 surface, which illustrated that the cadmium was doped on the g-C_3N_4 surface (Zhang et al. 2016). Fig. 3i illustrated the amorphous structure of 10-Cd-g-C_3N_4 sample. The selected diffraction pattern (Fig. 3j) shows two distinct amorphous diffraction rings, which correspond to two peaks of

carbon nitride in the XRD pattern and correspond to the XRD data. All these results clarified that 10-Cd-g-C_3N_4 samples were successfully constructed.

The BET specific surface area, pore volume and pore size distribution were tested by N_2 adsorption-desorption and the results were depicted in Table S3 and Fig. S2. The specific surface area of 10-Cd-g-C_3N_4 was 16.46 m^2/g, and the pore volume was 0.123 cm^3/g, whereas the surface area of pure g-C_3N_4 was 13.467 m^2/g, and the pore volume was 0.077 cm^3/g. Obviously, the 10-Cd-g-C_3N_4 sample obtained a larger surface area and pore volume than pure g-C_3N_4. Analogously, the porosity of 10-Cd-g-C_3N_4 was obviously increased, which related to the cracks of light layer during crystal growth process or the evaporation of chlorine gas during heating process. Undoubtedly, larger surface area and pore volume could provide more reaction active sites, increase abundant light absorption area and accelerate the transfer of photogenerated carriers, accordingly, achieving a higher photocatalytic degradation rate (Chang et al. 2015). The N_2 adsorption-desorption isotherm (Fig. S2a) of 10-Cd-g-C_3N_4 was exhibited a type IV curve with H3 hysteresis hoop, which represented the presence of slit shaped mesoporous structure (Iqbal et al. 2017).

The element chemical bonding states and electronic structure details were investigated by XPS analysis. Fig. 4a characterized the full survey spectrum of g-C_3N_4 and 10-Cd-g-C_3N_4. Obviously, the pure g-C_3N_4 sample was consisted of carbon (C), nitrogen (N), oxygen (O) element and the 10-Cd-g-C_3N_4 sample was consisted of C, N, O and cadmium (Cd) element. The presence of O element was caused by carbon nitride thermal polymerization process or catalyst surface absorption of water (Chou et al. 2016; Fang et al. 2016; Xue et al. 2019). Equally, no signal of chlorine (Cl) element (around 200 eV) could be observed, since Cl atoms were evaporated during heating process (Amirthaganesan et al. 2010).

The peaks of Cd 3d were situated at 405.6 eV and 412.4 eV in Fig. 4b, which were ascribed to the Cd $3d_{5/2}$ and Cd $3d_{3/2}$ (Reddy et al. 2021), indicating the existence of Cd^{2+} in 10-Cd-g-C_3N_4 (Zhang et al. 2016a), and further confirming the presence of Cd dopant (Abu Hanif et al. 2021). Similarly, Fig. 4c elucidated the high-resolution C1s spectra, two sharp peaks were situated at 284.8 and 288.3 eV, respectively. The former peak at 284.8 eV was specifically on behalf of carbon atoms (C–C bonds), namely graphite or amorphous carbon (Liu et al. 2010; Takanabe et al. 2010), and the latter sharper peak at 288.4 eV resulted from sp^2 C atoms bonded with adjacent N atoms inside the aromatic structure (N–C=N) (Thomas et al. 2008). Obviously, three peaks could be perceived from the high-resolution N 1s spectra (Fig. 4d), the peak at 398.8 eV originated from sp^2-bonded N atoms in triazine units (C=N–C) (Li et al. 2009b; Takanabe et al. 2010), the peak at 401.1 eV corresponded to amino groups (C–N–H) from the surface uncondensed bridging N atom (Liu et al. 2010; Thomas et al. 2008), which were similar to previously published literature (Chao et al. 2014; Matanović et al. 2015). The peak at 404 eV was assigned to the effects of surface charge localization in the heterocycles or the π–π* excitations between the stacking interlayers (Kong et al. 2018; Li et al. 2018; Zhang et al. 2014; Zhang et al. 2012). Both the high-resolution C 1s and N 1s spectra confirmed the presence of g-C_3N_4. Simultaneously, both C 1s and N 1s spectra of 10-Cd-g-C_3N_4 sample exhibited an upwards shifted compared with pure g-C_3N_4, all these

positive shifts could be ascribed to the electrons transfer of 10-Cd-g-C_3N_4 sample, further proving the strong interaction between Cd elements and g-C_3N_4 (Ji et al. 2019; Yan et al. 2019).

3.2. Optical properties

The optical absorption characteristics was an evaluation criterion to optical properties and electronic band structures of catalyst. Simultaneously, the optical absorption range and capacity of catalysts affected the photocatalytic performance. Fig. 5a revealed the UV–vis diffuse adsorption spectrum of g-C_3N_4 and 10-Cd-g-C_3N_4. An absorption threshold at 465 nm was found in pure g-C_3N_4. Obviously, the absorption threshold of 10-Cd-g-C_3N_4 had a significantly redshift toward longer wavelengths compared with pure g-C_3N_4, which illustrated that Cd doping may form a new level in g-C_3N_4 and cause a narrower band gap (Abu Hanif et al. 2021). Moreover, the intensity of light adsorption was significantly enhanced in 10-Cd-g-C_3N_4 sample, which further confirmed the improvement of light absorption performance. Additionally, 10-Cd-g-C_3N_4 extended the adsorption edges to near 600 nm, this extension is conducive to increasing the light absorption of g-C_3N_4 and increasing the generation of electron–hole pairs (Chen et al. 2021). Simultaneously, the UV–vis diffuse adsorption spectrum of other samples with different cadmium contents was clarified in Fig. S3a. Among these samples, the 10-Cd-g-C_3N_4 sample displayed the highest visible light absorption in a long range.

Both g-C_3N_4 and 10-Cd-g-C_3N_4 sample are direct-gap materials. The band gap (E_g) of g-C_3N_4 and 10-Cd-g-C_3N_4 were calculated based on the related Tauc plots in Fig. 5b (Luo et al. 2017). Noticeably, the band gap of pure g-C_3N_4 was assigned to 2.57 eV (Kong et al. 2018; Wang et al. 2009b; Zhang et al. 2012), and the band gap of 10-Cd-g-C_3N_4 was 2.29 eV. Undoubtedly, the narrower band gap reduced the excitation energy for photogenerated carriers, leading to a significant improvement in the visible light response. As a consequence, Cd doping can significantly affect the light absorption performance of g-C_3N_4 (Ge et al. 2012).

The charge separation, migration and recombination were analyzed. Fig. 6a indicated the PL spectra of 10-Cd-g-C_3N_4 and g-C_3N_4 samples. Commonly, the weakened PL intensity meant enhanced photoinduced charge separation and transfer efficiency. Apparently, the strong peak at 460 nm in pure g-C_3N_4 was consistent with the absorption edge of the UV-vis DRS, and indicating the severe recombination of the photogenerated electron–hole pair (Yu et al. 2013). Equally, the highest intensity peak demonstrated a red-shifted from 460 nm to 490 nm in 10-Cd-g-C_3N_4, which was associated with the band gap narrowing effect (Gu et al. 2018; Zou et al. 2019). Analogously, the PL spectra of other samples with different cadmium contents was manifested in Fig. S3b. Obviously, the PL spectra of Cd-g-C_3N_4 sample significantly fell with the doping of cadmium, which could ascribe to the fast interfacial charge migration. Additionally, the PL spectra of 10-Cd-g-C_3N_4 was lowest, which illustrated that Cd doping restrained the recombination of photoinduced charge due to the strong contact between cadmium and g-C_3N_4 (Thomas et al. 2008).

Figure 6b was a Mott-Schottky plots with flat band potentials at 1000 Hz. Commonly, conduction band potential is equivalent to flat band potential for an n-type semiconductor. Both g-C_3N_4 and 10-Cd-g-C_3N_4 displayed a positive slope, indicating g-C_3N_4 and 10-Cd-g-C_3N_4 are both n-type semiconductors. Meanwhile, the Mott-Schottky slope of 10-Cd-g-C_3N_4 was abated compare with pure g-C_3N_4, owing to the increased electrical conductivity and the quick mobility of charge carriers, which revealing the electron donor density was increased in 10-Cd-g-C_3N_4 (Jun et al. 2013; Pan et al. 2018; Yang et al. 2013; Yuan et al. 2018; Zhou et al. 2014). As a consequence, higher electron donor density is helpful for improving photocatalytic performance (Zhou et al. 2014). The conduction band potential of g-C_3N_4 and 10-Cd-g-C_3N_4 concluded from the Mott-Schottky plots was -0.84 eV and -1.02 eV, compared with Ag/AgCl electrodes, corresponding to -0.64 eV and -0.82 eV vs normal hydrogen electrode (NHE).

Metal elements doping influenced the band edge of catalyst to a great extent, and the redox capacity of semiconductors were evaluated via the band edge position of conduction (E_{CB}) and the valence (E_{VB}) (Xiong et al. 2016). The E_{VB} could obtained from following equation (Zhang et al. 2010):

$$E_{VB} = E_{CB} + E_g$$

Figure S4 revealed the E_{VB} and E_{CB} positions of as-prepared samples. For pure g-C_3N_4, the E_{VB} was 1.93 eV, on the basis of the experimental E_g (2.57 eV), the E_{CB} was -0.64 eV. Meanwhile, the E_{VB} of 10-Cd-g-C_3N_4 was 1.47 eV and the E_{CB} was -0.82 eV, according to the experimental E_g (2.29 eV).

Other photoelectrochemical techniques such as electrochemical impedance spectroscopy (EIS) and photocurrent response measurement were employed to investigate the movement of photoinduced electrons. Fig. 6c revealed the photocurrent responses of as-prepared samples, both g-C_3N_4 and 10-Cd-g-C_3N_4 testified an outstanding reproduceible photostability under successive on/off irradiation cycles. Homoplastically, the photocurrent response density of 10-Cd-g-C_3N_4 was significantly increased compare with pure g-C_3N_4, indicating the introduction of Cd element increased the conductivity of g-C_3N_4 and accelerated the separation of electron-hole pair (Ren et al. 2017). EIS was another method to evaluated the separation and transfer efficiency of photoinduced carriers. Commonly, the smaller arc radius suggested smaller transfer resistance, namely the better separation and transfer efficiency of photoinduced carriers (Lu et al. 2017; Yang et al. 2002). As depicted in Fig. 6d, the arc radius of 10-Cd-g-C_3N_4 was smaller than pure g-C_3N_4, which reflected that 10-Cd-g-C_3N_4 possessed high-efficiency photoinduced carriers separation ability and faster interfacial charge transfer level (Zhu et al. 2015).

3.3. Photocatalytic activities

To testing the effect of different content of Cd doping on degradation performance, a group of comparative degradation experiments were carried out under the simulated visible-light irradiation (λ > 420 nm). In this paper, TC was selected as contaminant because of the high stability under visible light. As illustrated in Fig. 7a, the degradation rate of TC without catalysts can be neglected. Apparently, the adsorption capacity of all Cd doped g-C_3N_4 samples were slightly larger than that of pure g-C_3N_4 during

the dark stage, which corresponding to an increase in the specific surface area of the catalyst. Obviously, all Cd doped g-C_3N_4 samples exhibits great increased photocatalytic degradation performance after 60 min visible-light irradiation compared with pure g-C_3N_4 (43.9%), confirming the doping of Cd was truly enhanced the photocatalytic efficiency (Abu Hanif et al. 2021). Apparently, the 10-Cd-g-C_3N_4 sample demonstrated the significantly improved photocatalytic degradation performance (98.1%), which can be attributed to the effective separation and transfer of photogenerated charges originating from the photocatalyst interface. Additionally, the photocatalytic degradation performance within 10 min of 10-Cd-g-C_3N_4 sample was tested (Fig. S5a), the result illustrated that the TC was degraded almost 80% within 10 minutes. Table S4 illustrated the comparison with other similar types researches, we found the removal rate of this work was excellent, by compare this work with other similar types of work.

Furthermore, the degradation performance of Cd doped g-C_3N_4 samples first enhanced with the increase of Cd content. As the content of Cd increased, the utility efficiency of visible light was promoted, as a consequence, more photoinduced carriers were provided. Unfortunately, when the doping content of Cd continuously increased, the degradation performance was decreased, the photocatalytic degradation performance of 15-Cd-g-C_3N_4 sample was only 75.9%, indicating the excessive Cd element could serve as photo-carrier's recombination center or blocked the surface active site to restrained the light absorption capacity and thus inhibiting photocatalytic degradation performance (Li et al. 2009a; Zhang et al. 2016b; Zhang et al. 2010).

The pseudo-first-order kinetic model could further investigate the degradation performance of the as-prepared catalyst, and the formula was expressed as follow:

$$\ln (C_t/C_0) = - K_{app}t$$

C_0 is the initial concentrations, C_t is the concentrations at time t, and K_{app} is reaction rate constant (min^{-1}), respectively. Fig. S5b presented the pseudo-first-order kinetic plots of Cd-g-C_3N_4 samples and pure g-C_3N_4. Under the same condition, the K_{app} of Cd-g-C_3N_4 samples were higher than pure g-C_3N_4 and the K_{app} of 10-Cd-g-C_3N_4 sample was the highest, demonstrating that 10-Cd-g-C_3N_4 had the best photocatalytic performance, which was consisted with the above experimental results.

The effects of different reaction conditions, such as initial concentration of TC, catalyst dosage and pH, were studied to meet practical application. Fig. 7b displayed the influence of different catalyst dosages on TC photodegradation. Apparently, as the catalyst dosages increased between 0.6 and 0.8 g/L, the removal rate of TC was enhanced monotonically, which was ascribed to the increased contact active sites between contaminants and materials, and more contaminants were absorbed on the surface of materials. Apparently, the catalyst dosages at 0.8 g/L elucidated the best photocatalytic degradation performance. Nevertheless, when the catalyst dosages over 0.8 g/L, the removal rate of TC was abated slightly, the photocatalytic degradation efficiency was 82.3% when the catalyst dosages at 1.0 g/L, which owing to the excessive catalyst reduced the photo-adsorption ability, as a result, hindering the effective migration of charge carriers (Zhang et al. 2016a).

The effect of different pH on TC photodegradation was clarified in Fig. 7c, and diluted hydrochloric acid and sodium hydroxide were used to adjust the initial pH. Obviously, the best degradation efficiency of TC was 94.4% at pH=5. Consequently, it was concluded that degradation efficiency was decreased in low pH values and alkaline environment, which can be explained by the surface charge of contaminants and materials. Additionally, the effect of initial concentration of TC was illuminated in Fig. 7d. It could be notably detected that the removal rates were abated with the initial concentration increased, and the best removal rate was 96.7% at 10 mg/L of TC. Two possible reasons could be proposed to elucidate this tendency. Firstly, high concentrations of contaminants might accumulate at the surface of catalyst, inhibiting the light absorption capacity. Secondly, intermediate products produced in the process of contaminants degradation might occupy the surface active site, so that contaminants had no contact with the catalyst.

In order to evaluated the practicability for catalysts, the stability tests were carried out by reusing the catalyst. Fig. 8a depicted the degradation rates of TC in four consecutive cycles. Obviously, the degradation rates were slightly decreased with the reuse of 10-Cd-g-C_3N_4, which could be attributed to the catalyst loss during the collection process. Whereas, the degradation rates still maintained a high level (89.5%) at the fourth cycle. Simultaneously, Fig. 8b demonstrated the XRD analysis of catalyst, no obvious peak changes were found in used catalyst, indicating the outstanding stability of 10-Cd-g-C_3N_4.

The ability of mineralization of note is an important index in photocatalytic process, which is used to ascertain the degree of contaminants removal. As intriguingly indicated in Fig. S4b, the mineralization efficiency of TC reached to 34% within 60 min visible light irradiation, which confirmed that 10-Cd-g-C_3N_4 could actually degrade TC into small molecule intermediate compounds (CO_2, H_2O).

3.4. Mechanism

The trapping experiments were used to determine the active species participating in the degradation process (Li et al. 2015). EDTA-2Na, IPA and TEMPO were added as scavengers to capture h^+, •OH and $•O_2^-$, respectively. Fig. 9a and Fig. 9b illustrated that the degradation rate of TC was suppressed by EDTA-2Na, indicating that h^+ was the main active species of 10-Cd-g-C_3N_4. Similarly, the degradation rate of TC abated slightly when the TEMPO and IPA were added, revealing that $•O_2^-$ and •OH played auxiliary roles in photocatalytic degradation process (Yan et al. 2010; Yu et al. 2018).

The ESR was carried out to verify the above results. As illustrated in Fig. 9c and Fig. 9d, it is hard to see the ups and downs signals of active species in 10-Cd-g-C_3N_4 under dark conditions. Paradoxically, the strong intensity 1:2:2:1 signals of •OH and 1:1:1:1 signals of $•O_2^-$ radicals could be found under the visible light irradiation, which proving the visible light is prerequisite for 10-Cd-g-C_3N_4 to product •OH and $•O_2^-$ active species.

According to all aforementioned results, the introduction of Cd element speeding up the separation and transfer of electron-hole pairs, decreasing the recombination rate of photogenerated charge carriers,

providing more reactive sites and accelerating cross-plane diffusion in g-C_3N_4 nanosheets (Iqbal et al. 2017), thus achieving the enhanced photocatalytic property. A brief mechanism of 10-Cd-g-C_3N_4 sample during TC degradation was summarized in Scheme 1. The electrons and holes were firstly generated and separated under light irradiation, and the electrons transferred from valence band to conduction band spontaneously, as a consequence, leaving holes at valence band and electrons accumulated at conduction band (Eq. (1)). Then, the absorbed O_2 reacted with electrons to formed superoxide radical (Eq. (2)). Similarly, the surplus electrons reacted with superoxide radical to formed hydrogen peroxide (H_2O_2) (Eq. (3)). As listed in Fig. S4a, the E_{CB} of 10-Cd-g-C_3N_4 was negative than $O_2/•O_2^-$ (-0.33 eV vs NHE), as a result, the accumulated electrons could react with O_2 to formed $•O_2^-$. But the E_{VB} of 10-Cd-g-C_3N_4 was negative than $OH^-/•OH$ (2.40 eV vs NHE), consequently, the accumulated holes could not react with OH^- to formed •OH, which was not consistent with ESR result. Consequently, the •OH probably derived from H_2O_2 decomposition (Eq. (4)). From what has been discussed above, $•O_2^-$, •OH and h^+ were worked together to degrade TC into small molecules (Eq. (5)). The reaction equations involved in the photocatalytic reaction process are manifested below (Jia et al. 2020).

10-Cd-g-C_3N_4 + hv → e^- + h^+ (1)

O_2 + e^- → $•O_2^-$ (2)

$•O_2^-$ + e^- + $2H^+$ → H_2O_2 (3)

H_2O_2 + e^- → •OH + OH^- (4)

$•O_2^-$ + h^+ + •OH + TC → H_2O + CO_2 + intermediate products (5)

4. Conclusion

In summary, the commendable 10-Cd-g-C_3N_4 photocatalyst were successfully prepared via oil bath by mixing dopant agent $CdCl_2$ with g-C_3N_4 in ethanol/H_2O solution. The degradation experiments demonstrated explicitly that the photocatalytic activity of g-C_3N_4 could be enhanced significantly with the doping of Cd element, and the best removal efficiency was 98.1% under visible light irradiation, which was 2.0-times enhanced in comparison with pure g-C_3N_4 (43.9%). Based on the characterization analysis, the enhanced photocatalytic performance could be ascribed to the following reasons: firstly, the enhanced photo-absorption ability, accelerating the migration, separation and transfer efficiency of photogenerated carriers. Meanwhile, the ultrathin mesoporous structure and the increased surface area could provide more active sites along with a shortened electron-transfer pathway, which was conducive to inhibiting the recombination of the photogenerated electrons and holes. As a consequence, this paper has demonstrated the 10-Cd-g-C_3N_4 sample can the significantly photocatalytic degradation tetracycline.

Declarations

Acknowledgements

This work was supported by the National Natural Science Foundation of China (52070077, U20A20323, 51521006, 51879101), the National Program for Support of Top–Notch Young Professionals of China (2014), the Program for Changjiang Scholars and Innovative Research Team in University (IRT-13R17), the Fundamental Research Funds for the Central Universities (531118010226).

Availability of data and materials All data generated or analyzed during the current study are included in this article and its supplementary information files.

Authors contributions YZ: Responsible for writing papers, conducting experiments, drawing the chart and analyzing the characterization part. HQ, ZW, HW, YH, QT, QL, PX: Responsible for reviewing the article and providing suggestions for revisions. The first draft of the manuscript was written by YZ and all authors commented on previous versions of the manuscript. All authors read and approved the final manuscript.”

Ethical approval Not applicable.

Consent to participate Not applicable.

Consent to publish Not applicable.

Competing interests The authors declare that they have no competing interests.

References

1. Abbott D (2010) Keeping the Energy Debate Clean: How Do We Supply the World's Energy Needs? Proceedings of the IEEE 98: 42-66. DOI: 10.1109/jproc.2009.2035162
2. Abu Hanif M, Akter J, Akherul Islam M, Sapkota KP, Hahn JR (2021) Visible-light-driven enhanced photocatalytic performance using cadmium-doping of tungsten (VI) oxide and nanocomposite formation with graphitic carbon nitride disks. Appl Surf Sci 565:150541. DOI: 10.1016/j.apsusc.2021.150541
3. Amirthaganesan G, Dhanabal T, Nanthini K, Dhandapani M (2010) Thermal and FTIR spectral characterization of diammonium tetrachloromanganate (II) monohydrate crystals. Materials Letters - MATER LETT 64:264–266. DOI: 10.1016/j.matlet.2009.10.057
4. Butchosa C, Guiglion P, Zwijnenburg MA (2014) Carbon Nitride Photocatalysts for Water Splitting: A Computational Perspective. J Phys Chem C 118:24833–24842. DOI: 10.1021/jp507372n
5. Chai B, Peng T, Mao J, Li K, Zan L (2012) Graphitic carbon nitride (g-C_3N_4)-Pt-TiO_2 nanocomposite as an efficient photocatalyst for hydrogen production under visible light irradiation. Physical chemistry chemical physics - PCCP 14:16745–16752. DOI: 10.1039/c2cp42484c

6. Chan D, Yu J, Yecheng l, Hu Z (2017) A metal-free composite photocatalyst of graphene quantum dots deposited on red phosphorus. J Environ Sci 60:91–97. DOI: 10.1016/j.jes.2016.11.025
7. Chang F, Li C, Luo J, Xie Y, Deng B, Hu X (2015) Enhanced visible-light-driven photocatalytic performance of porous graphitic carbon nitride. Appl Surf Sci 358:270–277. DOI: 10.1016/j.apsusc.2015.08.124
8. Chang F, Yan W, Cheng W, Wu F, Deng B, Hu X (2018) The construction and enhanced photocatalytic performance of binary composite S/g-C_3N_4. Mater Sci Semicond Process 87:1–6. DOI: 10.1016/j.mssp.2018.07.005
9. Chao K, Liao H, Shyue J, Lian S-S (2014) Corrosion Behavior of High Nitrogen Nickel-Free Fe-16Cr-Mn-Mo-N Stainless Steels. Metall Mater Trans B 45:381–391. DOI: 10.1007/s11663-013-9891-z
10. Chen Q, Wan B, Zhu P, Xu S, Huang Y (2021) The synergy of adsorption and photosensitization of platinum-doped graphitic carbon nitride for improved removal of rhodamine B. Environmental Science and Pollution Research. : DOI: 10.1007/s11356-021-15340-0
11. Chen X, Peng X, Jiang L, Yuan X-Z, Yu H, Hou W, Zhang J, Xia Q (2020) Recent advances in titanium metal–organic frameworks and their derived materials: Features, fabrication, and photocatalytic applications. Chem Eng J 395:125080. DOI: 10.1016/j.cej.2020.125080
12. Chou S-Y, Chen C-C, Dai Y-M, Lin J-H, Lee WW (2016) Novel synthesis of bismuth oxyiodide/graphitic carbon nitride nanocomposites with enhanced visible-light photocatalytic activity. RSC Adv 6:33478–33491. DOI: 10.1039/c5ra28024a
13. Dong G, Zhao K, Zhang L (2012) Carbon self-doping induced high electronic conductivity and photoreactivity of g-C_3N_4. Chemical communications (Cambridge, England). 48:6178–6180.. DOI: 10.1039/c2cc32181e
14. Fan J, Qin H, Jiang S (2019) Mn-doped g-C_3N_4 composite to activate peroxymonosulfate for acetaminophen degradation: The role of superoxide anion and singlet oxygen. Chem Eng J 359:723–732. DOI: 10.1016/j.cej.2018.11.165
15. Fan M, Cj S, Chen T, Yan X, Dongbo X, Gu W, Shi W, xiao l (2016) Visible-Light-Drived High Photocatalytic Activities of Cu/g-C_3N_4 photocatalysts for Hydrogen Production. RSC Adv 6:34633–34640. DOI: 10.1039/c5ra27755h
16. Fang LJ, Wang XL, Zhao JJ, Li YH, Wang YL, Du XL, He ZF, Zeng HD, Yang HG (2016) One-step fabrication of porous oxygen-doped g-C_3N_4 with feeble nitrogen vacancies for enhanced photocatalytic performance. Chem Commun 52:14408–14411. DOI: 10.1039/c6cc08187h
17. Gao H, Yan S, Wang J, Huang YA, Wang P, Li Z, Zou Z (2013) Towards efficient solar hydrogen production by intercalated carbon nitride photocatalyst. Physical Chemistry Chemical Physics 15:18077–18084. DOI: 10.1039/c3cp53774a
18. Gao J, Zhou Y, Li Z, Yan S, Wang N, Zou Z (2012) High-yield synthesis of millimetre-long, semiconducting carbon nitride nanotubes with intense photoluminescence emission and reproducible photoconductivity. Nanoscale 4:3687–3692. DOI: 10.1039/c2nr30777d

19. Ge L, Han C, Liu J, Li Y (2011) Enhanced visible light photocatalytic activity of novel polymeric g-C_3N_4 loaded with Ag nanoparticles. Appl Catal A 409–410:215–222. DOI: 10.1016/j.apcata.2011.10.006
20. Ge L, Zuo F, Liu J, Ma Q, Wang C, Sun D, Bartels L, Feng P (2012) Synthesis and Efficient Visible Light Photocatalytic Hydrogen Evolution of Polymeric g-C_3N_4 Coupled with CdS Quantum Dots. J Phys Chem C 116:13708–13714. DOI: 10.1021/jp3041692
21. Gu Y, Yu Y, Zou J, Shen T, Xu Q, Yue X, Meng J, Wang J (2018) The ultra-rapid synthesis of rGO/g-C_3N_4 composite via microwave heating with enhanced photocatalytic performance. Mater Lett 232:107–109. DOI: 10.1016/j.matlet.2018.08.077
22. Huang D, Chen S, Zeng G, Gong X, Zhou C, Cheng M, Xue W, Yan X, Li J (2019) Artificial Z-scheme photocatalytic system: What have been done and where to go? Coord Chem Rev 385:44–80. DOI: 10.1016/j.ccr.2018.12.013
23. Iqbal W, Dong C, Xing M, Tan X, Zhang J (2017) Eco-friendly one-pot synthesis of well-adorned mesoporous g-C_3N_4 with efficiently enhanced visible light photocatalytic activity. Catal Sci Technol 7:1726–1734. DOI: 10.1039/c7cy00286f
24. Ji C, Du C, Steinkruger JD, Zhou C, Yang S (2019) In-situ hydrothermal fabrication of CdS/g-C_3N_4 nanocomposites for enhanced photocatalytic water splitting. Mater Lett 240:128–131. DOI: 10.1016/j.matlet.2018.12.128
25. Jia J, Jiang C, Zhang X, Li P, Xiong J, Zhang Z, Wu T, Wang Y (2019) Urea-modified carbon quantum dots as electron mediator decorated g-C_3N_4/WO_3 with enhanced visible-light photocatalytic activity and mechanism insight. Appl Surf Sci 495:143524. DOI: 10.1016/j.apsusc.2019.07.266
26. Jia J, Zhang X, Jiang C, Huang W, Wang Y (2020) Visible-light-driven nitrogen-doped carbon quantum dots decorated g-C_3N_4/Bi_2WO_6 Z-scheme composite with enhanced photocatalytic activity and mechanism insight. J Alloys Compd 835:155180. DOI: 10.1016/j.jallcom.2020.155180
27. Jun Y-S, Lee E, Wang X, Hong W, Stucky G, Thomas A (2013) From Melamine-Cyanuric Acid Supramolecular Aggregates to Carbon Nitride Hollow Spheres. Adv Funct Mater 23(29):3661–3667. DOI: 10.1002/adfm.201203732
28. Katsumata H, Sakai T, Suzuki T, Knaeco S (2014) Highly Efficient Photocatalytic Activity of g-C_3N_4/Ag_3PO_4 Hybrid Photocatalysts through Z-Scheme Photocatalytic Mechanism under Visible Light. Ind Eng Chem Res 53:8018–8025. DOI: 10.1021/ie5012036
29. Kong L, Yujin J, Dang Z, Yan J, Li P, Li Y (2018) g-C_3N_4 Loading Black Phosphorus Quantum Dot for Efficient and Stable Photocatalytic H_2 Generation under Visible Light. Adv Funct Mater 28:1800668. DOI: 10.1002/adfm.201800668
30. Li H, Liu Y, Gao X, Fu C, Wang X (2015) Facile Synthesis and Enhanced Visible-Light Photocatalysis of Graphitic Carbon Nitride Composite Semiconductors. Chemsuschem 8:7:1189–1196. DOI: 10.1016/j.cattod.2017.05.017

31. Li H, Shan C, Pan B (2018) Fe(III)-Doped g-C_3N_4 Mediated Peroxymonosulfate Activation for Selective Degradation of Phenolic Compounds via High-Valent Iron-Oxo Species. Environ Sci Technol 52:2197–2205. DOI: 10.1021/acs.est.7b05563
32. Li J, Xu J, Dai W-L, Li H, Fan K (2009a) Direct hydro-alcohol thermal synthesis of special core–shell structured Fe-doped titania microspheres with extended visible light response and enhanced photoactivity. Appl Catal B 85:162–170. DOI: 10.1016/j.apcatb.2008.07.008
33. Li X, Zhang J, Shen L, Yanmei m, Lei W, Cui Q, Zou G (2009b) Preparation and characterization of graphitic carbon nitride through pyrolysis of melamine. Appl Phys A 94:387–392. DOI: 10.1007/s00339-008-4816-4
34. Li Z, Liu Z, Li B, Li D, Ge C, Fang Y (2016) Novel CdS nanorods/g-C_3N_4 nanosheets 1-D/2-D hybrid architectures: an in situ growth route and excellent visible light photoelectrochemical performances. J Mater Sci: Mater Electron 27:2904–2913. DOI: 10.1007/s10854-015-4108-7
35. Liu G, Niu P, Smith S, Chen Z-G, Lu M, Cheng H-M (2010) Unique Electronic Structure Induced High Photoreactivity of Sulfur-Doped Graphitic C_3N_4. J Am Chem Soc 132:11642–11648. DOI: 10.1021/ja103798k
36. Liu J, Liu Y, Naiyun L, Han Y, Zhang X, Huang H, Lifshitz Y, Lee S-T, Zhong J, Kang ZH (2015) ChemInform Abstract: Metal-Free Efficient Photocatalyst for Stable Visible Water Splitting via a Two-Electron Pathway. Science (New York, N.Y.) 347: 970-4. DOI: 10.1126/science.aaa3145
37. Liu S, Li D, Sun H, Ang HM, Tadé MO, Wang S (2016) Oxygen functional groups in graphitic carbon nitride for enhanced photocatalysis. J Colloid Interface Sci 468:176–182. DOI: 10.1016/j.jcis.2016.01.051
38. Liu W, Wang M, Xu C, Chen S (2012) Facile synthesis of g-C_3N_4/ZnO composite with enhanced visible light photooxidation and photoreduction properties. Chem Eng J 209:386–393. DOI: 10.1016/j.cej.2012.08.033
39. Liu Y, He M, Guo R, Fang Z, Kang S, Ma Z, Dong M, Wang W, Cui L (2020) Ultrastable metal-free near-infrared-driven photocatalysts for H_2 production based on protonated 2D g-C_3N_4 sensitized with Chlorine6. Appl Catal B 260:118137. DOI: 10.1016/j.apcatb.2019.118137
40. Lu Q, Deng J, Hou Y, Wang H, Li H, Zhang Y (2015) One-step electrochemical synthesis of ultrathin graphitic carbon nitride nanosheets and their application to the detection of uric acid. Chem Commun 51:12251–12253. DOI: 10.1039/c5cc04231c
41. Lu Z, Song W, Ouyang C, Wang H, Zeng D, Xie C (2017) Enhanced visible-light photocatalytic performance of highly-dispersed Pt/g-C_3N_4 nanocomposites by one-step solvothermal treatment. RSC Adv 7:33552–33557. DOI: 10.1039/c7ra04931e
42. Luo L, Zhang A, Janik MJ, Li K, Song C, Guo X (2017) Facile fabrication of ordered mesoporous graphitic carbon nitride for RhB photocatalytic degradation. Appl Surf Sci 396:78–84. DOI: 10.1016/j.apsusc.2016.10.190

43. Matanović I, Babanova S, Iii A, Serov A, Artyushkova K, Atanassov P (2015) Bio-inspired Design of Electrocatalysts for Oxalate Oxidation: a Combined Experimental and Computational Study of Mn-N-C Catalyst. Phys Chem Chem Phys 17:13235–13244. DOI: 10.1039/c5cp00676g
44. McCauley S, Stephens J (2012) Green energy clusters and socio-technical transitions: Analysis of a sustainable energy cluster for regional economic development in Central Massachusetts, USA. Sustain Sci 7:213–225. DOI: 10.1007/s11625-012-0164-6
45. Narkbuakaew T, Sujaridworakun P (2020) Synthesis of Tri-S-Triazine Based g-C_3N_4 Photocatalyst for Cationic Rhodamine B Degradation under Visible Light. Top Catal 63:1086–1096. DOI: 10.1007/s11244-020-01375-z
46. Ong W-J, Tan L-L, Ng YH, Yong S-T, Chai S-P (2016) Graphitic Carbon Nitride (g-C_3N_4)-Based Photocatalysts for Artificial Photosynthesis and Environmental Remediation: Are We a Step Closer To Achieving Sustainability? Chem Rev 116:7159–7329. DOI: 10.1021/acs.chemrev.6b00075
47. Ou M, Zhong Q, Zhang S, Yu L (2015) Ultrasound assisted synthesis of heterogeneous g-C_3N_4/$BiVO_4$ composites and their visible-light-induced photocatalytic oxidation of NO in gas phase. J Alloys Compd 626:401–409. DOI: 10.1016/j.jallcom.2014.11.148
48. Pan J, Feng S, Zhao C, Dong Z, Wang B, Wang J, Song C, Zheng Y, Li C (2018) The enhanced photocatalytic hydrogen production of the fusiform g-C_3N_4 modification $CaTiO_3$ nano-heterojunction. Int J Hydrog Energy 43(14):19019–19028. DOI: 10.1016/j.ijhydene.2018.08.102
49. Park S-S, Chu S-W, Xue C, Zhao D, Ha C-S (2011) Facile synthesis of mesoporous carbon nitrides using the incipient wetness method and the application as hydrogen adsorbent. J Mater Chem 21:10801–10807. DOI: 10.1039/c7ra02178j
50. Qi Y, Liang Q, Lv R, Shen W, Kang F, Huang Z-H (2018) Synthesis and photocatalytic activity of mesoporous g-C_3N_4/MoS_2 hybrid catalysts. R Soc Open Sci 5:180187–180187. DOI: 10.1098/rsos.180187
51. Reddy NR, Reddy PM, Mandal TK, Yedluri AK, Joo SW (2021) Architecture of superior hybrid electrode by the composition of Cu_2O nanoflakes, novel cadmium ferrite ($CdFe_2O_4$) nanoparticles, and g-C_3N_4 sheets for symmetric and asymmetric supercapacitors. Journal of Energy Storage 43:103302. DOI: 10.1016/j.est.2021.103302
52. Ren K, Yin P, Zhou Y, Cao X, Dong C, Cui L, Liu H, Du X (2017) Localized Defects on Copper Sulfide Surface for Enhanced Plasmon Resonance and Water Splitting. Small 13:1700867. DOI: 10.1002/smll.201700867
53. Samanta S, Martha S, Parida K (2014) Facile Synthesis of Au/g-C_3N_4 Nanocomposites: An Inorganic/Organic Hybrid Plasmonic Photocatalyst with Enhanced Hydrogen Gas Evolution Under Visible-Light Irradiation. ChemCatChem 6,5: 1453-1462. DOI: 10.1002/cctc.201300949
54. Schwinghammer K, Mesch M, Duppel V, Ziegler C, Senker J, Lotsch B (2014) Crystalline Carbon Nitride Nanosheets for Improved Visible-Light Hydrogen Evolution. J Am Chem Soc 136(5):1730–1733. DOI: 10.1021/ja411321s

55. Sher M, Javed M, Shahid S, Iqbal S, Qamar MA, Bahadur A, Qayyum MA (2021) The controlled synthesis of g-C_3N_4/Cd-doped ZnO nanocomposites as potential photocatalysts for the disinfection and degradation of organic pollutants under visible light irradiation. RSC Adv 11:2025–2039. DOI: 10.1016/j.est.2021.103302
56. Shi J, Chen G, Zeng G, Chen A, He K, Huang Z, Hu L, Zeng J, Wu J, Liu W (2018) Hydrothermal synthesis of graphene wrapped Fe-doped TiO_2 nanospheres with high photocatalysis performance. Ceram Int 44:7473–7480. DOI: 10.1016/j.ceramint.2018.01.124
57. Sobhana SSL, Devi M, Sastry T, Mandal A (2011) CdS quantum dots for measurement of the size-dependent optical properties of thiol capping. J Nanopart Res 13:1747–1757. DOI: 10.1007/s11051-010-9934-1
58. Song B, Chen M, Ye S, Xu P, Zeng G, Gong J, Li J, Zhang P, Cao W (2019) Effects of multi-walled carbon nanotubes on metabolic function of the microbial community in riverine sediment contaminated with phenanthrene. Carbon 144:1–7. DOI: 10.1016/j.carbon.2018.12.016
59. Tahir M, Cao C, Butt F, Mahmood A, Idrees F, Hussain S, Tanveer M, Ali Z, Aslam I (2013) Multifunctional g-C3N4 Nanofibers: A Template-Free Fabrication and Enhanced Optical, Electrochemical, and Photocatalyst Properties. ACS Appl Mater Interfaces 6(2):1258–1265. DOI: 10.1021/am405076b
60. Takanabe K, Kamata K, Wang X, Antonietti M, Kubota J, Domen K (2010) Photocatalytic hydrogen evolution on dye-sensitized mesoporous carbon nitride photocatalyst with magnesium phthalocyanine. Phys Chem Chem Phys 12:13020–13025. DOI: 10.1039/c0cp00611d
61. Thaweesak S, Wang S, Lyu M, Xiao M, Peerakiatkhajohn P, Wang L (2017) Boron-doped graphitic carbon nitride nanosheets for enhanced visible-light driven photocatalytic water splitting. Dalton Trans 46:10714–10720. DOI: 10.1039/c7dt00933j
62. Tonda S, Kumar S, Kandula S, Shanker V (2014) Fe-doped and -mediated graphitic carbon nitride nanosheets for enhanced photocatalytic performance under natural sunlight. Journal of Materials Chemistry A: Materials for Energy and Sustainability 2:6772. DOI: 10.1039/c3ta15358d
63. Wang H, Wang H, Wang Z, Tang L, Zeng G, Xu P, Chen M, Xiong T, Zhou C, Li X, Huang D, Zhu Y, Wang Z, Tang J (2020a) Covalent organic framework photocatalysts: structures and applications. Chem Soc Rev 49:4135–4165. DOI: 10.1039/d0cs00278j
64. Wang Q, Yang Z (2016) Industrial water pollution, water environment treatment, and health risks in China. Environ Pollut 218:358–365. DOI: 10.1016/j.envpol.2016.07.011
65. Wang W, Xu P, Chen M, Zeng G, Zhang C, Zhou C, Yang Y, Huang D, Lai C, Cheng M, Hu L, Xiong W, Guo H, Zhou M (2018a) Alkali Metal-Assisted Synthesis of Graphite Carbon Nitride with Tunable Band-Gap for Enhanced Visible-Light-Driven Photocatalytic Performance. ACS Sustain Chem Eng 6:15503–15516. DOI: 10.1021/acssuschemeng.8b03965
66. Wang X, Maeda K, Thomas A, Takanabe K, Xin G, Carlsson J, Domen K, Antonietti M (2008) A metal-free polymeric photocatalyst for hydrogen production from water under visible light. Nat Mater 8:76–80. DOI: 10.1038/nmat2317

67. Wang X, Chen X, Thomas A, Fu X, Antonietti M (2009a) Metal-Containing Carbon Nitride Compounds: A New Functional Organic–Metal Hybrid Material. Adv Mater 21:1609–1612. DOI: 10.1002/adma.200802627
68. Wang X, Maeda K, Thomas A, Takanabe K, Xin G, Carlsson JM, Domen K, Antonietti M (2009b) A metal-free polymeric photocatalyst for hydrogen production from water under visible light. Nat Mater 8:76–80. DOI: 10.1038/nmat2317
69. Wang Y, Yang W, Chen X, Wang J, Zhu Y (2018b) Photocatalytic activity enhancement of core-shell structure g-C_3N_4@TiO_2 via controlled ultrathin g-C_3N_4 layer. Appl Catal B 220:337–347. DOI: 10.1016/j.apcatb.2017.08.004
70. Wang Z, Chen M, Huang D, Zeng G, Xu P, Zhou C, Lai C, Wang H, Cheng M, Wang W (2019) Multiply structural optimized strategies for bismuth oxyhalide photocatalysis and their environmental application. Chem Eng J 374:1025–1045. DOI: 10.1016/j.cej.2019.06.018
71. Wang Z, Wang H, Zeng Z, Zeng G, Xu P, Xiao R, Huang D, Chen X, He L, Zhou C, Yang Y, Wang Z, Wang W, Xiong W (2020b) Metal-organic frameworks derived $Bi_2O_2CO_3$/porous carbon nitride: A nanosized Z-scheme systems with enhanced photocatalytic activity. Appl Catal B 267:118700. DOI: 10.1016/j.apcatb.2020.118700
72. Wang Z, Han W, Wang Z, Huang D, Qin H, He Y, Chen M, Zeng G, Xu P (2021) Ferrocene modified g-C_3N_4 as a heterogeneous catalyst for photo-assisted activation of persulfate for the degradation of tetracycline. Colloids Surf, A 626:127024. DOI: 10.1016/j.colsurfa.2021.127024
73. Xiang Q, Yu J, Jaroniec M (2012) Synergetic effect of MoS_2 and graphene as cocatalysts for enhanced photocatalytic H_2 production activity of TiO_2 nanoparticles. J Am Chem Soc 134:6575–6578. DOI: 10.1016/j.materresbull.2015.12.009
74. Xiao J-D, Jiang H-L (2017) Thermally Stable Metal-Organic Framework-Templated Synthesis of Hierarchically Porous Metal Sulfides: Enhanced Photocatalytic Hydrogen Production. Small (Weinheim an der Bergstrasse, Germany) 13,28: 1700632.. DOI: 10.1002/smll.201700632
75. Xiong T, Cen W, Zhang Y, Dong F (2016) Bridging the g-C_3N_4 Interlayers for Enhanced Photocatalysis. ACS Catal 6:4: 2462–2472. DOI: 10.1021/acscatal.5b02922
76. Xu P, Chen M, Lai C, Zeng G, Huang D, Wang H, Gong X, Qin L, Liu Y, Mo D, Wen X, Zhou C, Wang R (2019) Effects of typical engineered nanomaterials on 4-nonylphenol degradation in river sediment: based on bacterial community and function analysis. Environmental Science: Nano 6:2171–2184. DOI: 10.1039/c9en00371a
77. Xue X, Chen R, Yan C, Hu Y, Zhang W, Yang S, Ma L, Zhu G, Jin Z (2019) Efficient photocatalytic nitrogen fixation under ambient conditions enabled by the heterojunctions of n-type Bi2MoO6 and oxygen-vacancy-rich p-type BiOBr. Nanoscale 11:10439–10445. DOI: 10.1039/c9nr02279a
78. Yan J, Zhou C, Li P, Chen B, Zhang S, Dong X, Xi F, Liu J (2016) Nitrogen-rich graphitic carbon nitride: Controllable nanosheet-like morphology, enhanced visible light absorption and superior photocatalytic performance. Colloids Surf, A 508:257–264. DOI: 10.1016/j.colsurfa.2016.08.067

79. Yan S, Li Z, Zou Z (2009a) Photodegradation Performance of g-C_3N_4 Fabricated by Directly Heating Melamine. Langmuir 25:10397–10401. DOI: 10.1021/la900923z
80. Yan S, Li Z, Zou Z (2010) Photodegradation of Rhodamine B and Methyl Orange over Boron-Doped g-C_3N_4 under Visible Light Irradiation. Langmuir 26:3894–3901. DOI: 10.1021/la904023j
81. Yan SC, Li ZS, Zou ZG (2009b) Photodegradation performance of g-C_3N_4 fabricated by directly heating melamine. Langmuir 25:10397–10401. DOI: 10.1021/la900923z
82. Yan W, Yan L, Jing C (2019) Impact of doped metals on urea-derived g-C_3N_4 for photocatalytic degradation of antibiotics: Structure, photoactivity and degradation mechanisms. Appl Catal B 244:475–485. DOI: 10.1016/j.apcatb.2018.11.069
83. Yang S, Gong Y, Zhang J, Zhan L, Ma L, Fang Z, Vajtai R, Wang X, Ajayan PM (2013) Exfoliated Graphitic Carbon Nitride Nanosheets as Efficient Catalysts for Hydrogen Evolution Under Visible Light. Adv Mater 25:2452–2456. DOI: 10.1002/adma.201204453
84. Yang W, Wang J, Pan T, Xu J, Zhang J, Cao C-n (2002) Studies on the electrochemical characteristics of $K_2Sr(FeO_4)_2$ electrode. Electrochem Commun 4:710–715. DOI: 10.1016/s1388-2481(02)00429-0
85. Yu J, Wang S, Low J, Xiao W (2013) Enhanced photocatalytic performance of direct Z-scheme g-C_3N_4–TiO_2 photocatalysts for the decomposition of formaldehyde in air. Physical Chemistry Chemical Physics 15:16883–16890. DOI: 10.1039/c3cp53131g
86. Yu Y, Wang J (2015) Direct microwave synthesis of graphitic C_3N_4 with improved visible-light photocatalytic activity. Ceram Int 42:4063–4071. DOI: 10.1016/j.ceramint.2015.11.078
87. Yu Y, Zhou Q, Wang J (2016) Ultra-rapid synthesis of 2D graphitic carbon nitride nanosheets via direct microwave heating for field emission. Chem Commun 52:3396–3399. DOI: 10.1039/c5cc10258h
88. Yu Y, Wang C, Luo L, Wang J, Meng J (2018) An environment-friendly route to synthesize pyramid-like g-C_3N_4 arrays for efficient degradation of rhodamine B under visible-light irradiation. Chem Eng J 334:1869–1877. DOI: 10.1016/j.cej.2017.11.133
89. Yuan J, Liu X, Tang Y, Zeng Y, Wang L, Zhang S, Cai T, Liu Y, Luo S, Pei Y, Liu C (2018) Positioning cyanamide defects in g-C_3N_4: Engineering energy levels and active sites for superior photocatalytic hydrogen evolution. Appl Catal B 237:24–31. DOI: 10.1016/j.apcatb.2018.05.064
90. Yuan Y-p, Yin L, Cao S, Gu L, Xu G, Du P, Chai H, Liao Y, Xue C (2014) Microwave-Assisted Heating Synthesis: A General and Rapid Strategy for Large-Scale Production of High Crystalline g-C_3N_4 with Enhanced Photocatalytic H_2 Production. Green Chem 16:4663–4668. DOI: 10.1039/c4gc01517g
91. Zhang C, Lu Y, Jiang Q, Hu J (2016a) Synthesis of CdS hollow spheres coupled with g-C_3N_4 as efficient visible-light-driven photocatalysts. Nanotechnology 27:355402. DOI: 10.1088/0957-4484/27/35/355402
92. Zhang C, Lu Y, Jiang Q, Hu J (2016b) Synthesis of CdS hollow spheres coupled with g-C_3N_4 as efficient visible-light-driven photocatalysts. Nanotechnology 27:355402. DOI: 10.1088/0957-4484/27/35/355402

93. Zhang G, Zhang M, Ye X, Qiu X, Lin S, Wang X (2014) Iodine Modified Carbon Nitride Semiconductors as Visible Light Photocatalysts for Hydrogen Evolution. Adv Mater 26:805–809. DOI: 10.1002/adma.201303611
94. Zhang J, Grzelczak M, Hou Y, Maeda K, Domen K, Fu X, Antonietti M, Wang X (2012) Photocatalytic oxidation of water by polymeric carbon nitride nanohybrids made of sustainable elements. Chem Sci 3:443–446. DOI: 10.1039/c1sc00644d
95. Zhang K, Wang L, Sheng X, Ma M, Jung MS, Kim W, Lee H, Park JH (2016c) Tunable Bandgap Energy and Promotion of H_2O_2 Oxidation for Overall Water Splitting from Carbon Nitride Nanowire Bundles. Advanced Energy Materials 6,11:1502352. DOI: 10.1002/aenm.201502352
96. Zhang L, Huang F, Liang C, Zhou L, Zhang X, Pang Q (2016) Ultrasound exfoliation of g-C_3N_4 with assistance of cadmium ions and synthesis of CdS/g-C_3N_4 ultrathin nanosheets with efficient photocatalytic activity. J Taiwan Inst Chem Eng 60:643–650. DOI: 10.1016/j.jtice.2015.11.013
97. Zhang L, Xia Z (2011) Mechanisms of Oxygen Reduction Reaction on Nitrogen-Doped Graphene for Fuel Cells. J Phys Chem C 115:22: 11170–11176. DOI: 10.1021/jp201991j
98. Zhang X, Jing D, Guo L (2010) Effects of anions on the photocatalytic H_2 production performance of hydrothermally synthesized Ni-doped $Cd_{0.1}Zn_{0.9}S$ photocatalysts. Int J Hydrog Energy 35:7051–7057. DOI: 10.1016/j.ijhydene.2009.12.132
99. Zhao Y, Zhao F, Wang X, Xu C, Zhang Z, Shi G, Qu L (2014) Graphitic Carbon Nitride Nanoribbons: Graphene-Assisted Formation and Synergic Function for Highly Efficient Hydrogen Evolution. Angew Chem Int Ed 53:13934–13939. DOI: 10.1002/ange.201409080
100. Zhou W, Li W, Wang J-Q, Qu Y, Yang Y, Xie Y, Zhang K, Wang L, Fu H, Zhao D (2014) Ordered Mesoporous Black TiO_2 as Highly Efficient Hydrogen Evolution Photocatalyst. J Am Chem Soc 136:26: 9280–9283. DOI: 10.1021/ja504802q
101. Zhou X, Jin B, Chen R, Peng F, Fang Y (2013) Synthesis of porous Fe_3O_4/g-C_3N_4 nanospheres as highly efficient and recyclable photocatalysts. Mater Res Bull 48:1447–1452. DOI: 10.1016/j.materresbull.2012.12.038
102. Zhu J, Diao T, Wang W, Xu X, Sun X, Carabineiro SAC, Zhao Z (2017) Boron doped graphitic carbon nitride with acid-base duality for cycloaddition of carbon dioxide to epoxide under solvent-free condition. Appl Catal B 219:92–100. DOI: 10.1016/j.apcatb.2017.07.041
103. Zhu Y-P, Ren T-Z, Yuan Z-Y (2015) Mesoporous Phosphorus-Doped g-C_3N_4 Nanostructured Flowers with Superior Photocatalytic Hydrogen Evolution Performance. ACS Appl Mater Interfaces 7:16850–16856. DOI: 10.1021/acsami.5b04947
104. Zou J, Yu Y, Yan W, Meng J, Zhang S, Wang J (2019) A facile route to synthesize boron-doped g-C_3N_4 nanosheets with enhanced visible-light photocatalytic activity. J Mater Sci 54:867–6881. DOI: 10.1007/s10853-019-03384-0

Schemes

Scheme 1 are available in the Supplemental Files section

Figures

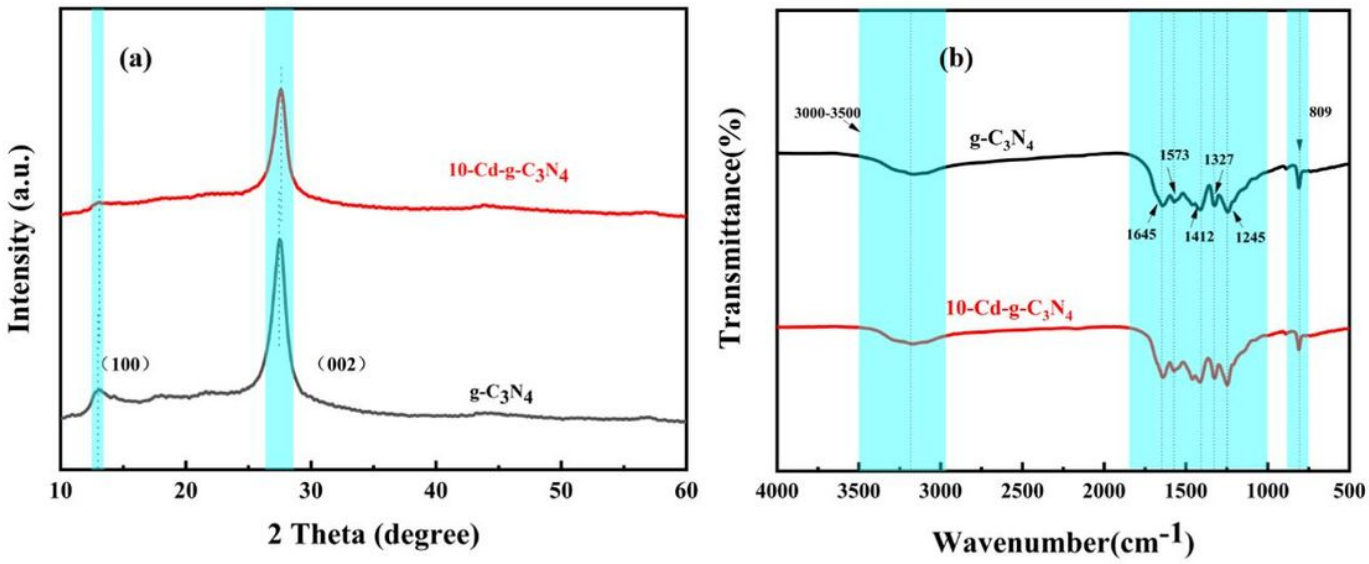

Figure 1

(a) XRD patterns of pure g-C_3N_4 and 10-Cd-g-C_3N_4 photocatalyst; (b) FT-IR spectra of pure g-C_3N_4 and 10-Cd-g-C_3N_4 photocatalyst.

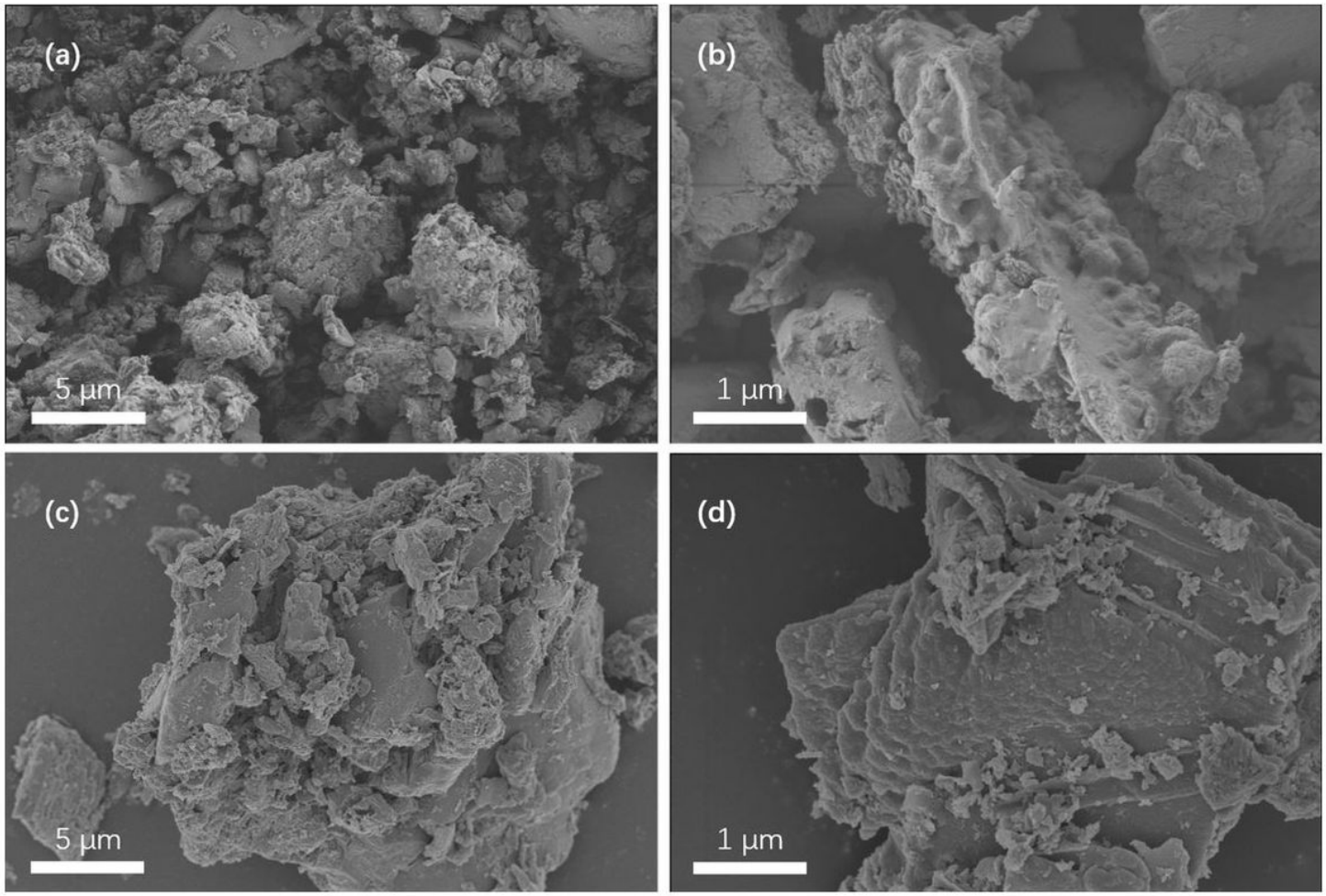

Figure 2

SEM images of g-C_3N_4 (a, b) and 10-Cd-g-C_3N_4 photocatalyst (c, d).

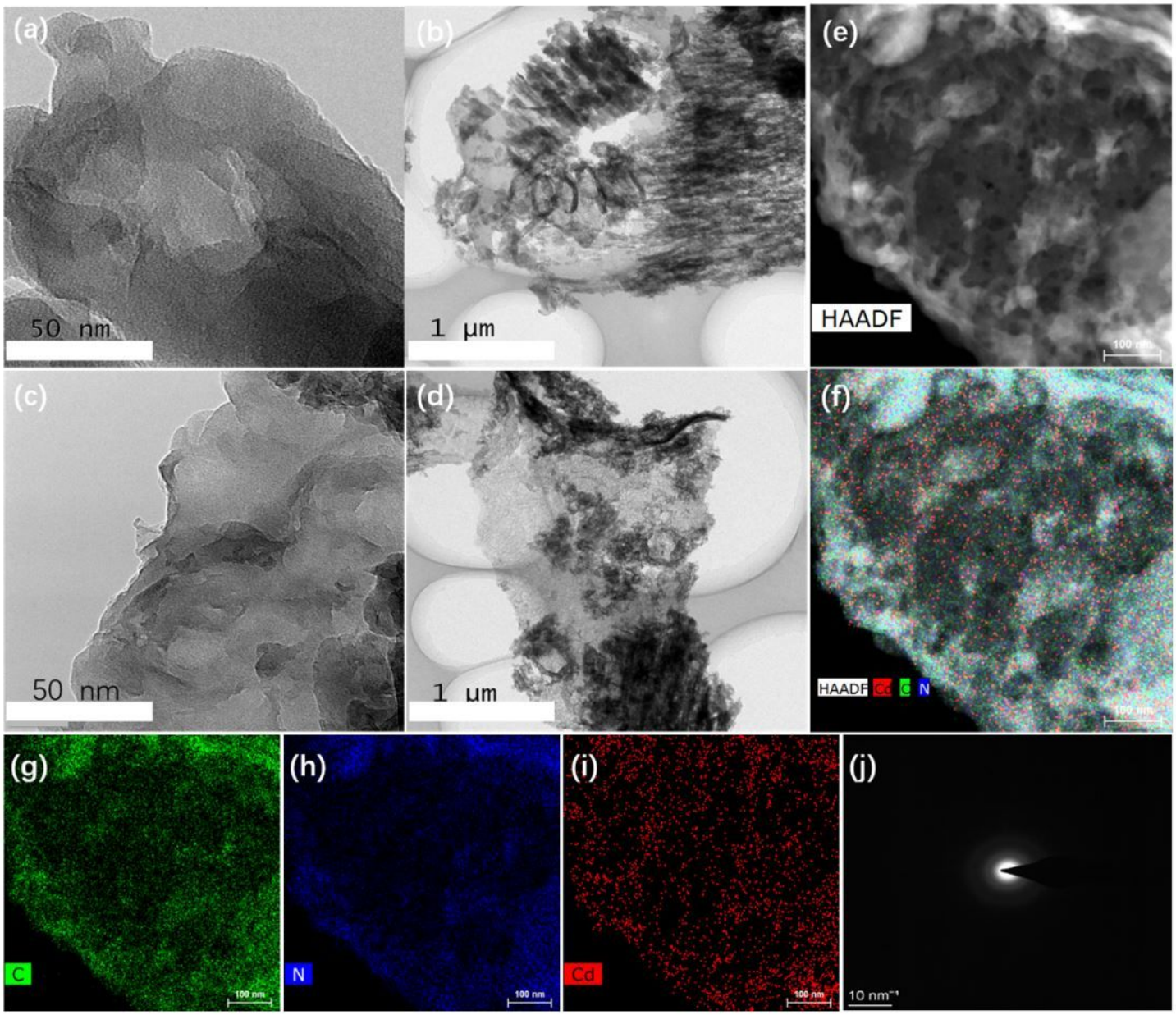

Figure 3

TEM images of g-C_3N_4 (a, b) and 10-Cd-g-C_3N_4 photocatalyst (c, d). HAADF-STEM, element mapping (e-i) and SAED images (j) of 10-Cd-g-C_3N_4.

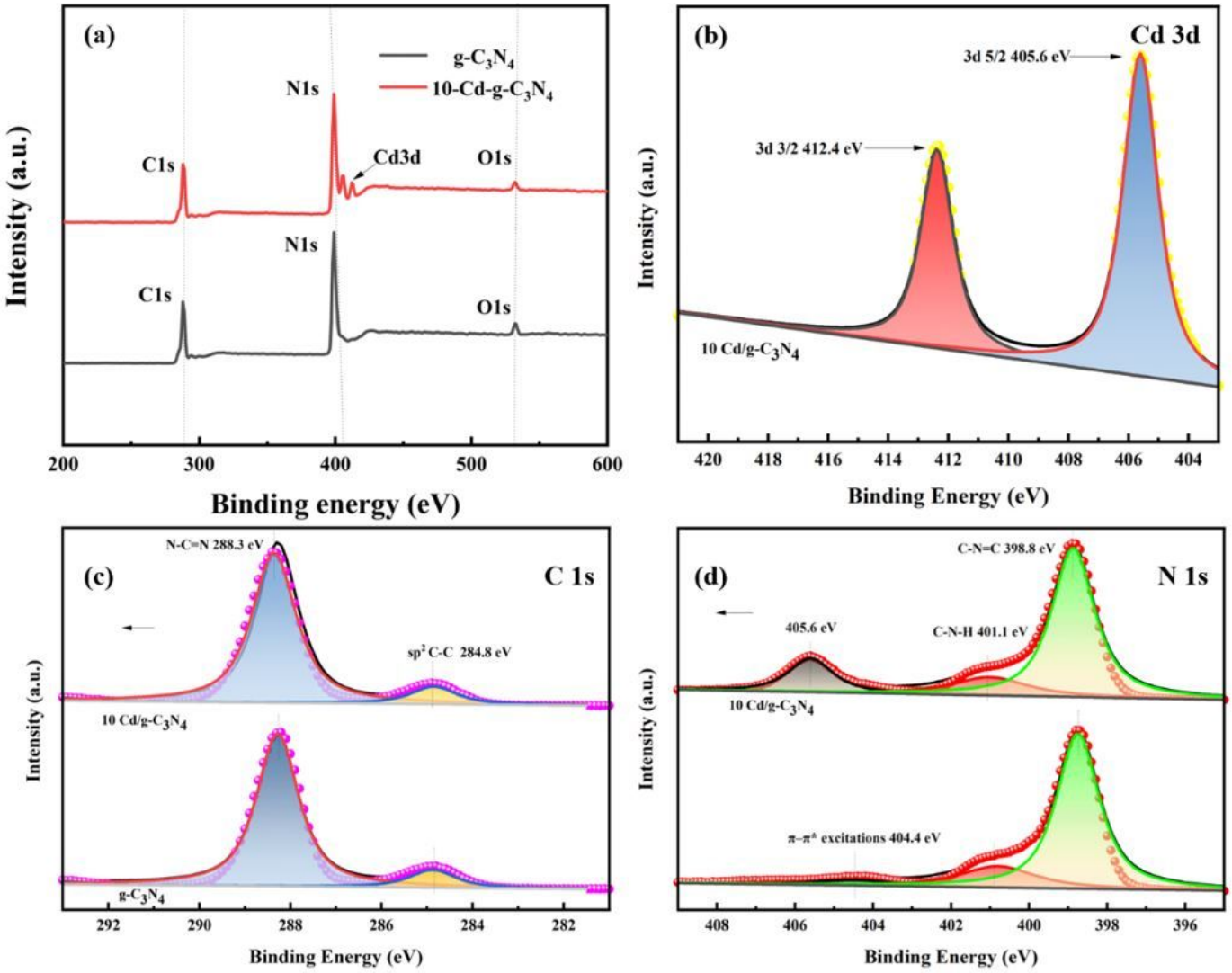

Figure 4

XPS spectra of pure g-C_3N_4 and 10-Cd-g-C_3N_4 photocatalyst. (a) full survey spectrum, (b) high-resolution Cd 3d, (c) high-resolution C 1s, (d) high-resolution N 1s.

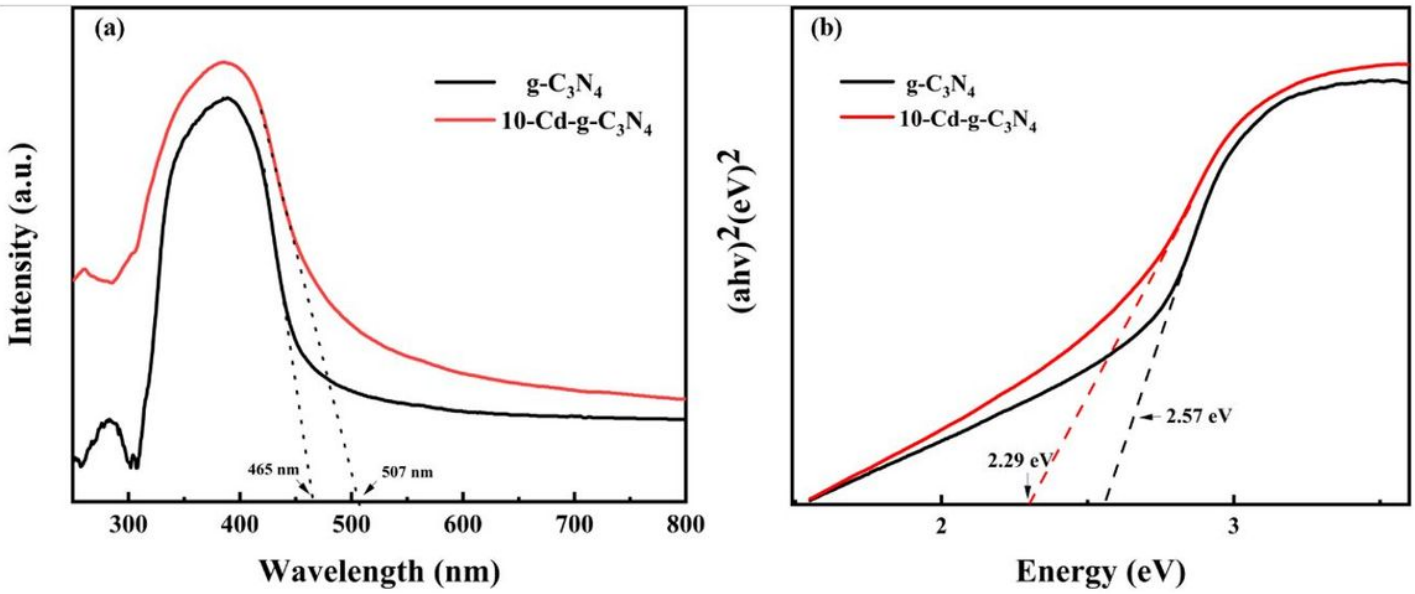

Figure 5

(a) UV–vis diffuse reflectance spectra (DRS) and (b) band gap of g-C_3N_4 and 10-Cd-g-C_3N_4 photocatalyst.

Figure 6

(a) The PL spectra and (b) Mott–Schottky plots of pure g-C_3N_4 and 10-Cd-g-C_3N_4 photocatalyst. (c) Photocurrent response spectra and (d) EIS Nyquist plots of pure g-C_3N_4 and 10-Cd-g-C_3N_4 photocatalyst.

Figure 7

(a) Degradation performance of catalysts curves with different amounts cadmium. Experimental conditions: $[Cd\text{-}g\text{-}C_3N_4]_0$ = 0.8 g L^{-1}, $[TC]_0$ = 10 mg L^{-1}, and T = 25 °C. (b) Degradation efficiency of different catalyst dosages. Experimental conditions: $[TC]_0$ = 10 mg L^{-1}, and T = 25 °C. (c) Degradation efficiency of 10-Cd-g-C_3N_4 composites with different pH. Experimental conditions: $[10\text{-}Cd\text{-}g\text{-}C_3N_4]_0$ = 0.8 g L^{-1}, $[TC]_0$ = 10 mg L^{-1}, and T = 25 °C. (d) Degradation efficiency of catalyst with different initial TC concentrations. Experimental conditions: $[10\text{-}Cd\text{-}g\text{-}C_3N_4]_0$ = 0.8 g L^{-1}, and T = 25 °C.

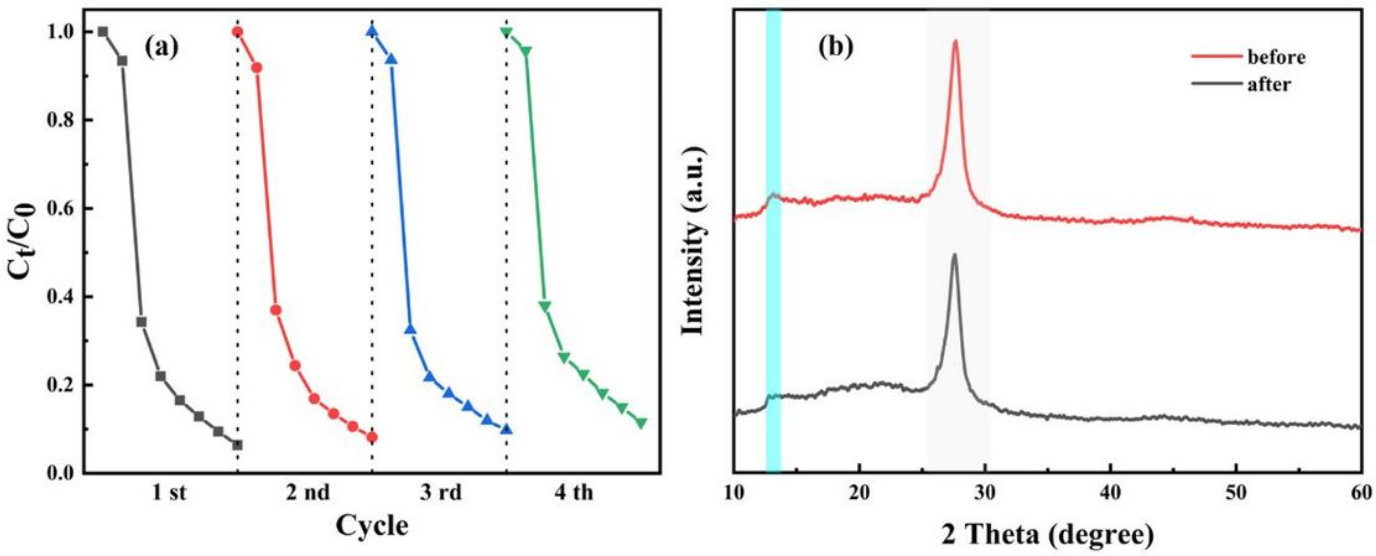

Figure 8

(a) Degradation efficiency of TC over 10-Cd-g-C_3N_4 photocatalyst under four cycling tests. (b) XRD images of 10-Cd-g-C_3N_4 photocatalyst before and after four times used. Experiments conditions: TC concentration = 20 mg/L; catalyst loading = 0.8 g/L, Temperature = 25℃.

Figure 9

(a, b) Degradation efficiency of 10-Cd-g-C_3N_4 photocatalyst under different quenchers. Experiments conditions: TC concentration = 20 mg/L; catalyst loading = 0.8 g/L, Temperature = 25℃. ESR spectra for (c) $DMPO^-$ •$O_2^-$and (d) $DMPO^-$ •OH under dark and visible light condition.

Supplementary Files

This is a list of supplementary files associated with this preprint. Click to download.

- Scheme1.jpg
- SupportingInformation.docx